ARTICLE IN PRESS

Available online at www.sciencedirect.com

ScienceDirect

Advances in Space Research xxx (xxxx) xxx

ADVANCES IN SPACE RESEARCH (a COSPAR publication)

www.elsevier.com/locate/asr

Comparison of satellite manoeuvre detection methods based on timeline of orbit elements

A. Zollo *, M. Weigel

German Aerospace Center (DLR), Space Operations and Astronaut Training, Oberpfaffenhofen, Germany

Received 17 February 2023; received in revised form 28 September 2023; accepted 21 October 2023

Abstract

This paper proposes two innovative methods for detecting satellite manoeuvres by analysing a timeline of orbit elements. The first one makes use of a Linear Kalman Filter (LKF) to track the evolution of orbit elements and identify changes, while the second one refers to a particular manoeuvre strategy of geostationary satellites and detects in-plane orbit corrections by evaluating differences in mean longitude. Their detection performances are compared to those of already-existing techniques and tested, when applicable, for both Low Earth Orbit (LEO) and Geostationary Earth Orbit (GEO) regimes. An optimization process is put in place to fairly confront different detection algorithms with distinct tuning parameters in order to ensure that every method is always providing its best detection performance. The defined loss function can also be used for a relative comparison of results, and this proves a better performance of the newly developed manoeuvre detection techniques.

Keywords: Satellite Manoeuvre Detection; Discrete Linear Kalman Filter; Space Surveillance

1. Introduction

The increasing number of operational satellites, along with the rapid growth of the in-orbit debris population over the last few decades, has given great importance to the topic of manoeuvre detection. Methods for finding artificial changes in the orbital state of a space object are usually categorized by the literature in real-time (or quasi-real time) detection and off-line detection processes. The algorithms belonging to the first category are often used by orbit catalogues to maintain and update the orbital state of regularly tracked satellites. One of the biggest challenges associated to a Space Situational Awareness catalogue is, in fact, the process of orbit determination of active satellites when no manoeuvre information is available a priori (Weigel et al., 2015; Zollo, 2020). This may lead to non-converged solutions with a consecutive loss of information about the satellite state or deteriorated orbit accuracy. Real-time manoeuvre detection usually involves the usage of a sequential estimator that determines, measurement by measurement, the orbital state of a space object. At each step the propagated state is converted to measurement space and compared to the next sensor observation. If the measurement residuals appear to be larger than a given threshold a manoeuvre is detected (Folcik et al., 2008; Bergmann et al., 2021, 2022; Zollo, 2020). Upon detection, the time of boost and the manoeuvre components are usually refined by respectively propagating and back-propagating the estimated orbit state bracketing the detected manoeuvre time. In this process quantities such as the relative distance or the probability of collision (Herzog et al., 2017), treating the two estimated states as if belonging to two different objects, are observed to refine the mean manoeuvring time, which in turn can be used by a

* Corresponding author.
E-mail addresses: andrea.zollo@dlr.de (A. Zollo), martin.weigel@dlr.de (M. Weigel).

https://doi.org/10.1016/j.asr.2023.10.032
0273-1177/

Please cite this article as: A. Zollo and M. Weigel, Comparison of satellite manoeuvre detection methods based on timeline of orbit elements, Advances in Space Research, https://doi.org/10.1016/j.asr.2023.10.032

batched least square estimator to determine the manoeuvre 'dv-component'.

The other branch of manoeuvre detection algorithms, defined as off-line, is what this research work aims to tackle. For this category, the orbit of the satellite is apriori estimated with respect to the detection process. The input data is, in fact, a timeline of historical orbital parameter of objects for which no manoeuvre information is available. Off-line analysis is quite useful to support real-time or quasi real-time manoeuvre detection for active objects that are regularly tracked. In fact, manoeuvre patterns, types and magnitude can be roughly forecasted in advance to help sensor scheduling and planning of tracking facilities (Siminski et al., 2017).

Detection techniques which are dealing with historical orbit data can in turn be divided in two subgroups. The first category has a more data-driven approach where a time series of orbit elements, or derived quantities, are processed and smoothed. Subsequent statistical analysis is then employed to distinguish when the points of the series become outliers with respect to the rest of the signal (Águeda et al., 2013; Patera, 2008; Song et al., 2012; Swartz et al., 2010; Schild and Noomen, 2022). The most representative example of such kind of algorithms is given by the work of Kelecy et al., where a sliding-window technique computes differences in orbital energy or in semi-major axis comparing segments of fitted data. The second subgroup involves ephemeris comparison by means of state vector propagation. A published state is propagated to the epochs of the neighbouring ones to assert if a manoeuvre happened. An example is given by the TLE consistency check algorithm (TCC), proposed by (Lemmens and Krag, 2014), where the spatial difference between two consecutive published states is checked to evaluate the dynamics consistency in absence of manoeuvres. Different work has been carried out recently following the same philosophy of the TCC, focusing the attention on the propagation part (Mukundan and Wang, 2021) and how considerations on the prediction error can adjust the detection threshold for noise interference removal (Li et al., 2018, 2019).

In this framework, we are proposing two innovative techniques: the first one, described in Section 2 and enhanced in Section 3, makes use of an LKF to understand when the predicted state of a tracked orbital element diverges the most from the next datapoint in the time-sequence. The second one, in Section 4, refers to a particular manoeuvre strategy for the in-plane control of geostationary satellites. In this case, smoothed differences in mean longitude are analysed to find manoeuvres. Section 5 details the detection process with the introduction of the peak prominence as a discrimination threshold to distinguish manoeuvres from the background noise of the signal. Subsequently, Section 6 introduces the optimization process we adopted to fairly compare the performance of our newly developed methods to the work of Kelecy et al. (2007) and Lemmens and Krag (2014). Finally, the results, for different test cases of LEO and GEO satellites, are illustrated in Sections 7, 8 and 9.

2. Discrete-time LKF for event detection

We are proposing to use a discrete-time LKF (Kalman, 1960) to detect satellite manoeuvres by processing an already established timeline of orbit elements. The concept behind the method is to consider the LKF as a means to smooth noisy data and to detect sudden changes in the orbital state rather than actually estimate it.

A timeline of orbit elements, being the result of a routine orbit determination process, serves as input data. Selected orbit elements and derived quantities are considered for establishing a set of measurements to be ingested sequentially by the filter. The semi-major axis can be tracked to find orbit changes due to in-plane orbit manoeuvres, while changes in inclination directly point to out-of-plane manoeuvres. The estimated orbit states will vary temporally, with trends introduced by the different orbit perturbations. Therefore, the filter may also track time rates of the considered orbit elements that are introduced in the predict-step of the algorithm using linearized dynamics. The principle of a predictor–corrector sequential estimator is illustrated in Fig. 1.

The state of tracked orbit elements x_{t-1} at time stamp $t-1$ is propagated up to the measurement epoch t according to the following three cases:

$$\bar{x}_t = \begin{cases} x_{t-1} & (constant\ \ elements) \\ x_{t-1} + \dot{x}_{t-1}\Delta t & (constant\ \ rate\ \ of\ \ change) \\ x_{t-1} + \dot{x}_{t-1}\Delta t + \frac{1}{2}\ddot{x}_{t-1}\Delta t^2 & (constant\ \ acceleration) \end{cases} \tag{1}$$

where quantities with bars indicate a prior probability distribution and quantities without bars indicate a posterior probability distribution. The propagated state $\bar{x}_t$ is directly compared to the measurement z at epoch t in the computation of the residuals y. These are defined as the differences between the current filter prediction and the measurement, the residuals will be large for sensor observations after burns start till the filter converged to new orbit state.

In addition, supposing that state and measurements are expressed by multivariate gaussian distributions, and modelling the noise in the predict-step and in the measurements as white gaussian, one can expect the residuals to be centred around zero. As a consequence, when the satellite is not manoeuvring, the measurements $\boldsymbol{z}(t)$ will be given by the sum of the prior $\bar{\boldsymbol{x}}_t$ and the measurement noise $\boldsymbol{w}(t)$, supposing that state space and measurement space are equal. On the other hand, once the satellite starts manoeuvring, the next measurement will no longer be close to the prediction, indicated by:

$$\boldsymbol{z}(t) = \bar{\boldsymbol{x}}_t + \boldsymbol{w}(t) + \boldsymbol{\delta}(t) \tag{2}$$

where $\boldsymbol{\delta}(t)$ represents the increment due to the manoeuvre. For this, the residuals will be large and not centered around

Please cite this article as: A. Zollo and M. Weigel, Comparison of satellite manoeuvre detection methods based on timeline of orbit elements, Advances in Space Research, https://doi.org/10.1016/j.asr.2023.10.032

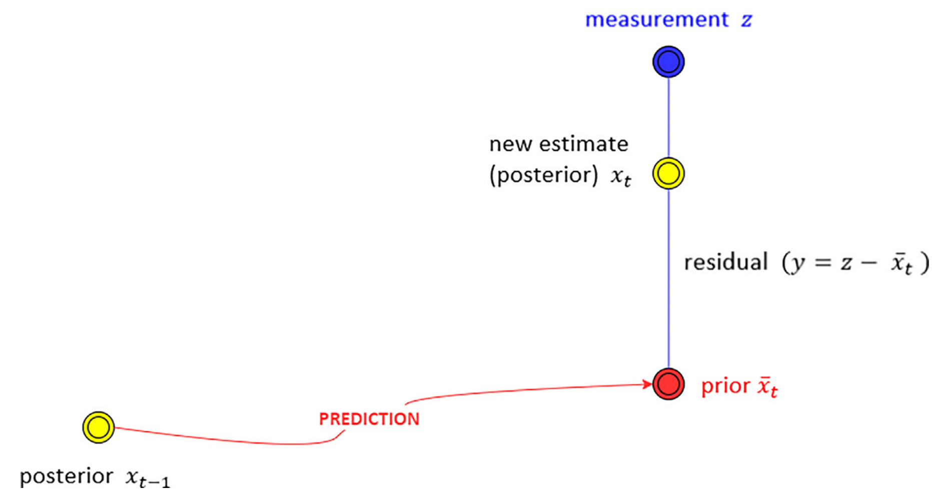

Fig. 1. Illustration of predictor–corrector algorithm.

zero anymore. Manoeuvres can thus be detected by analysing when the residuals start to diverge from a mean of zero (Labbe, 2020).

We detail below the mathematical formulation of a generic in-plane manoeuvre detection algorithm with an LKF of first order. For this purpose, a timeline of semi-major axes (a) is processed. Eq. (3) defines respectively the state vector $\boldsymbol{x_t}$, the state covariance matrix $\boldsymbol{P}$, the state transition matrix $\boldsymbol{F}$, the input matrix $\boldsymbol{B}$, the input vector $\boldsymbol{u}$, the process noise matrix $\boldsymbol{Q}$, the measurement $\boldsymbol{z}$, the measurement noise matrix $\boldsymbol{R}$ and the measurement function $\boldsymbol{H}$ as:

$$\begin{aligned}&\boldsymbol{x_t} = \begin{bmatrix} a_t \\ \dot{a}_t \end{bmatrix}, \quad \boldsymbol{F} = \begin{bmatrix} 1 & \Delta t \\ 0 & 1 \end{bmatrix}, \quad \boldsymbol{P} = \begin{bmatrix} \sigma_a^2 & \sigma_{a\dot{a}} \\ \sigma_{\dot{a}a} & \sigma_{\dot{a}}^2 \end{bmatrix},\\ &\boldsymbol{B} = 0, \quad \boldsymbol{u} = 0, \quad \boldsymbol{Q} = f(\Delta t, VAR)\\ &\boldsymbol{z} = [z], \quad \boldsymbol{R} = [\sigma_z^2], \quad \boldsymbol{H} = [10]\end{aligned} \tag{3}$$

In detail, at each time t the state vector tracks the semi-major axis estimates a_t and eventually its derivatives $(\dot{a}_t, \ddot{a}_t)$ depending on the simplified dynamics chosen from Eq.1. The matrix $\boldsymbol{F}$ propagates the state across subsequent time-intervals. The matrix $\boldsymbol{B}$ and the input vector $\boldsymbol{u}$ represent usually a modelled manoeuvre in the dynamics. These two entities will be always zero for our application since the objective is to spot manoeuvres without any apriori information. The matrix $\boldsymbol{P}$ represent the uncertainty of the estimates of a_t and its eventual time derivatives. The quantity $\boldsymbol{z}$ represents the measurement at each data epoch. For this case, the measurements coincide with the timeline of semi-major axis and, because of this, the mapping function $\boldsymbol{H}$ that usually performs the conversion from state-space to measurement space is equal to 1. $\boldsymbol{R}$ represents the uncertainty associated to the measurements and finally $\boldsymbol{Q}$ is a matrix that adds white noise to the state-transition process and depends on the Δt and the variance (VAR) of the white noise spectral density.

The predict-step of the algorithm can be expressed by the following set of equations:

$$\begin{cases} \bar{\boldsymbol{x}} = \boldsymbol{F}\boldsymbol{x} + \boldsymbol{B}\boldsymbol{u} \\ \bar{\boldsymbol{P}} = \boldsymbol{F}\boldsymbol{P}\boldsymbol{F}^{\boldsymbol{T}} + \boldsymbol{Q} \end{cases} \tag{4}$$

while the update-step is given by:

$$\begin{cases} \boldsymbol{y} = \boldsymbol{z} - \boldsymbol{H}\bar{\boldsymbol{x}} \\ \boldsymbol{K} = \bar{\boldsymbol{P}}\boldsymbol{H}^{\boldsymbol{T}}(\boldsymbol{H}\bar{\boldsymbol{P}}\boldsymbol{H}^{\boldsymbol{T}} + \boldsymbol{R})^{-1} \\ \boldsymbol{x} = \bar{\boldsymbol{x}} + \boldsymbol{K}\boldsymbol{y} \\ \boldsymbol{P} = (\boldsymbol{I} - \boldsymbol{K}\boldsymbol{H})\bar{\boldsymbol{P}} \end{cases} \tag{5}$$

As mentioned above, the major indicator of a manoeuvre happening is the divergence of the signal $\boldsymbol{y}$ from its mean. Despite this, it is worth mentioning that other derived metrics of the filter, often related to its performance evaluation, as the log-likelihood or the Mahalanobis distance (Mahalanobis, 1936) can also be evaluated to detect manoeuvres. In the framework of this research, we are analysing two parameters. The first quantity serves for normalization of the residuals $\boldsymbol{y}$, as proposed by (Bar-Shalom et al., 2001):

$$\boldsymbol{\varepsilon} = \boldsymbol{y}\boldsymbol{S}\boldsymbol{y}^{\boldsymbol{T}} \tag{6}$$

where ε represents the squared residuals, normalized with respect to the system uncertainty $\boldsymbol{S}$. The usage of this quantity to detect a manoeuvre is advantageous because the resulting peaks of its time evolution are always positive and their height is always normalized with respect to the local system uncertainty and independent from physical units. This means that their prominence, and in turn their detectability, is less sensitive to the applied filter design, settings and resulting filter performance.

As a second parameter, the filter tracks the rate of change in semi-major axis $\dot{a}$. This trend information improves the filter prediction, and therefore increases the signal-to-noise level for the detection of changes in semi-major axis. On the other hand, the tracked time rate may also be processed for change detection with the advantage of noise cancelation by the filter. The second technique, being more sensible to semi-major axis variations, has been used for most of the LEO test cases, where the magnitude of the manoeuvres to detect is usually less pronounced.

3. Smoothing procedure

The filter estimates can be further processed by means of fixed-interval smoothing, where the state is re-computed at each data epoch using all available previous and future measurements. Although many fixed-lag smoothers are available in the literature, the authors have chosen to use the so-called Rauch-Tung-Striebel (RTS) smoothing algorithm proposed in Rauch et al. (1965) because of its ease of implementation and computational efficiency.

The RTS smoother functioning principle requires as input the Kalman filter estimates of the state along with the covariance matrix for each predict/update step. It then processes the data backwards, incorporating its knowledge of the future into the past measurements. As a result, the smoothed signal presents generally less noise and the detection procedure benefits from it. The predict step can be reformulated with the following:

$$\boldsymbol{P} = \boldsymbol{F}\boldsymbol{P}_k\boldsymbol{F}^T + \boldsymbol{Q} \tag{7}$$

The update step assumes the following form:

$$\begin{cases} \boldsymbol{K}_k = \boldsymbol{P}_k\boldsymbol{F}^T\boldsymbol{P}^{-1} \\ \boldsymbol{x}_k = \boldsymbol{x}_k + \boldsymbol{K}_k(\boldsymbol{x}_{k+1} - \boldsymbol{F}\boldsymbol{x}_k) \\ \boldsymbol{P}_k = \boldsymbol{P}_k + \boldsymbol{K}_k(\boldsymbol{P}_{k+1} - \boldsymbol{P})\boldsymbol{K}_k^T \end{cases} \tag{8}$$

The reader is invited to note that, with respect to the nominal Kalman Filter equations, Eqs. (7) and (8) are introducing the subscripts k to distinguish between future and current data.

4. Mean-Longitude Filter (MLF) for bi-pulse East-West manoeuvre strategy

In case there are strict constraints on the eccentricity drift control of a GEO mission, the East-West correction of the spacecraft is usually performed by implementing a bi-pulse manoeuvre strategy, where the eccentricity vector and the longitude drift are corrected concurrently (Li, 2014; Montenbruck and Gill, 2001). Theoretically, after the two pulses, the satellite is brought back to the initial semi-major axis before the manoeuvres. This means that, before and after the dual pulses, there are no differences in semi-major axis or in specific orbital energy to be detected.

Changes in these two quantities will reveal manoeuvres only if sufficient observations for orbit determination are provided between the bi-pulses that usually are performed within the same day. We are then proposing a detection algorithm that considers the mean longitude. This last will in fact be altered, even after the relative drift is stopped by the second in-plane pulse.

In Fig. 2, the data processing workflow for the E-W control manoeuvres is shown. The mean longitude $\bar{\lambda}$ is computed at each epoch. Since $\bar{\lambda}$ depends on time and is therefore specific for each epoch of the orbit elements, the mean longitude is propagated up to the epoch of the next element set according to either analytical or numerical orbit propagation methods. The first case has the advantage of being computationally efficient, without the need to involve time-consuming numerical orbit integration:

$$\bar{\lambda}(t_k) = \bar{\lambda}(t_{k-1}) + n\Delta t \tag{9}$$

where n and Δt are respectively the mean motion and the time between two consecutives element sets. The differences in longitude $\Delta\bar{\lambda}_k$ at a given epoch k are then retrieved by comparing $\bar{\lambda}_{k-1}$ propagated up to k with the non-propagated $\bar{\lambda}_k$ as illustrated in Fig. 3. The output of this step is a timeline of differences in mean longitude that can be further processed to erase noise.

The differences are thus smoothed using a Locally Weighted Regression (LOWESS) routine (Cleveland, 1979). Fig. 4 shows in detail how to each raw data point a new smoothed y-value is assigned. Looping over the raw $\Delta\bar{\lambda}_k$, the algorithm computes the new fitted value by performing a polynomial fit to adjacent datapoints using weighted regression. The weights are assigned by shifting the following bell-shaped kernel function over the data:

$$f(t) = e^{\frac{-(t-t_k)^2}{\tau^2}} \tag{10}$$

The weighting depends on the time difference $(t - t_k)$ between adjacent datapoints to prioritise the values in proximity of the kernel function center. The parameter τ controls the width of the bell curve and is expressed as a fraction of the total number of data points.

Fig. 5 shows, for the case of the geostationary satellite METEOSAT-10, a time series of filtered mean longitude differences derived by TLE data published on Space-Track.org. It is important to note how the filter produces a smoothed curve up to the mean manoeuvring times (red vertical lines in figure) provided by the satellite operator EUMETSAT. After the onset of the manoeuvre, well defined spikes are arising in the filter output.

5. Detection process with peak prominence

The detection process requires most of the times an analysis of a signal time evolution, from which some peaks have to be distinguished with respect to the background noise. This last, for already-estimated orbit elements, is representing the uncertainty associated to a given orbit determination process, including at the same time measurement noise and noise introduced by the dynamical modelling. As already mentioned, the signals to be processed are always representing a time-line of differences in orbital parameters and their divergence from the general evolution

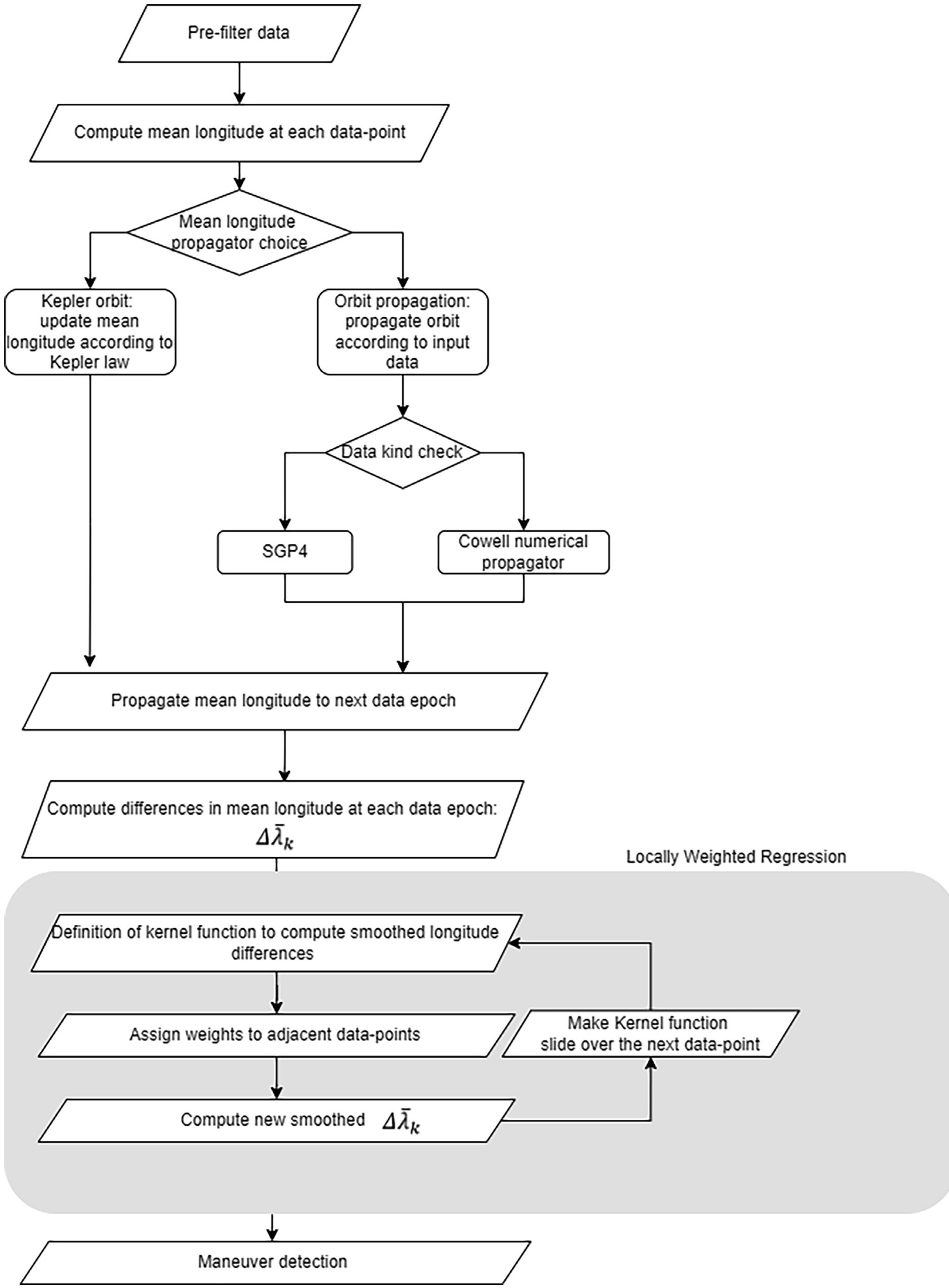

Fig. 2. Data processing workflow of mean longitude filter algorithm.

indicates a presumed manoeuvre. With regards to the detection of the peaks, the approach found from literature (Kelecy et al., 2007; Lemmens and Krag, 2014; Zhao et al., 2014) is to set some statistical limits in terms of mean and

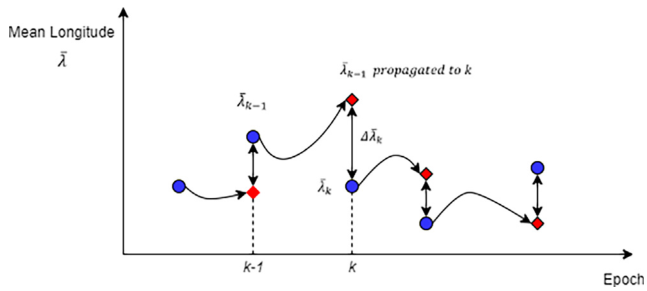

Fig. 3. Illustration of mean longitude filter algorithm.

standard deviation above which an orbit change is detected. The authors are instead proposing to make use of the peak prominence as a fair threshold for time-evolution data. The topographic prominence is used in mountain topography to measure the height of a peak relative to the lowest contour line encircling it but containing no higher summit within it. Its usage is advantageous especially when it comes to confront different signals belonging to different manoeuvres. The topographic prominence is in fact defined also for negative peaks and adapts better to several detection situations. For instance, a time-line of orbit elements with orbit raising and lowering manoeuvres or East-West (North-South) manoeuvring patterns with both positive and negative peaks can be detected defining only one threshold. On the contrary, dealing with two different thresholds based on the signal statistics increases the complexity when implementing the optimization process to compare the filters presented in Section 6.

Fig. 6 presents an example of a difficult detection situation for which the usage of the peak prominence is beneficial. One of the data-sets used within the framework of this research (see Table 2) is the case of the satellite BIROS controlled by the German Space Operation Centre (GSOC). From December 2016 to August 2017 a series of orbit-lowering manoeuvres were performed by the spacecraft. As shown, evaluating differences in semi-major axis with

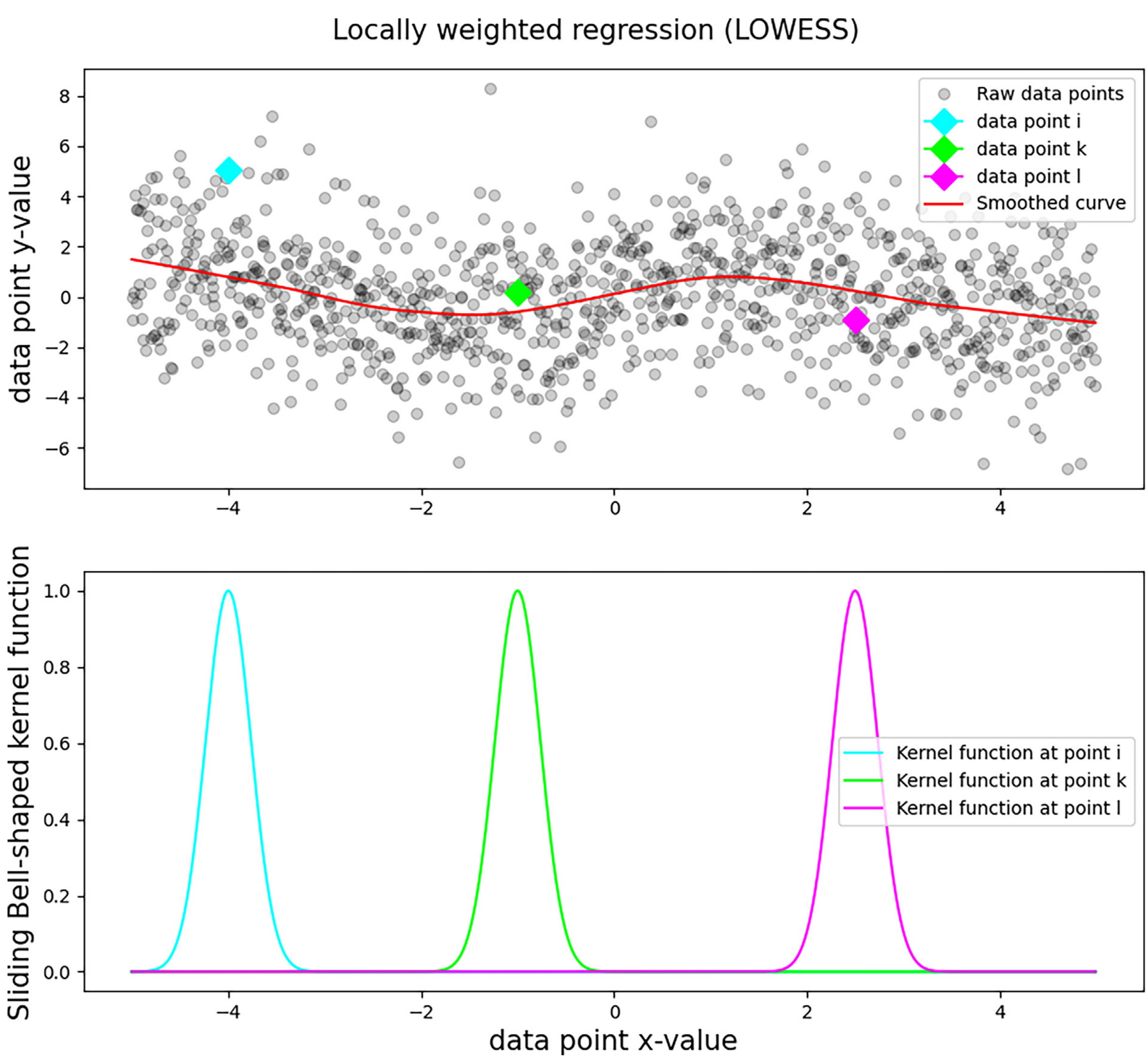

Fig. 4. Locally weighted regression with representation of sliding Bell-shaped kernel function on a general scatterplot.

Please cite this article as: A. Zollo and M. Weigel, Comparison of satellite manoeuvre detection methods based on timeline of orbit elements, Advances in Space Research, https://doi.org/10.1016/j.asr.2023.10.032

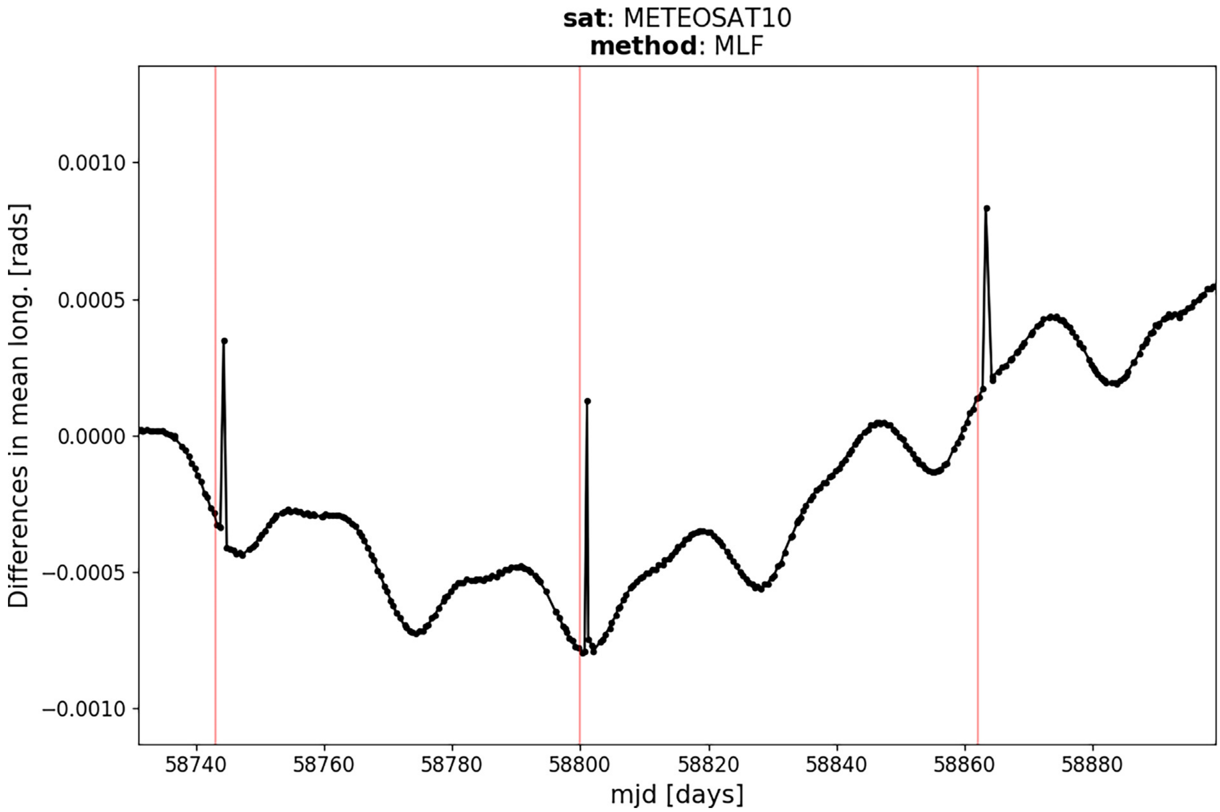

Fig. 5. Example results of Mean Longitude Filter (MLF) for METEOSAT-10.

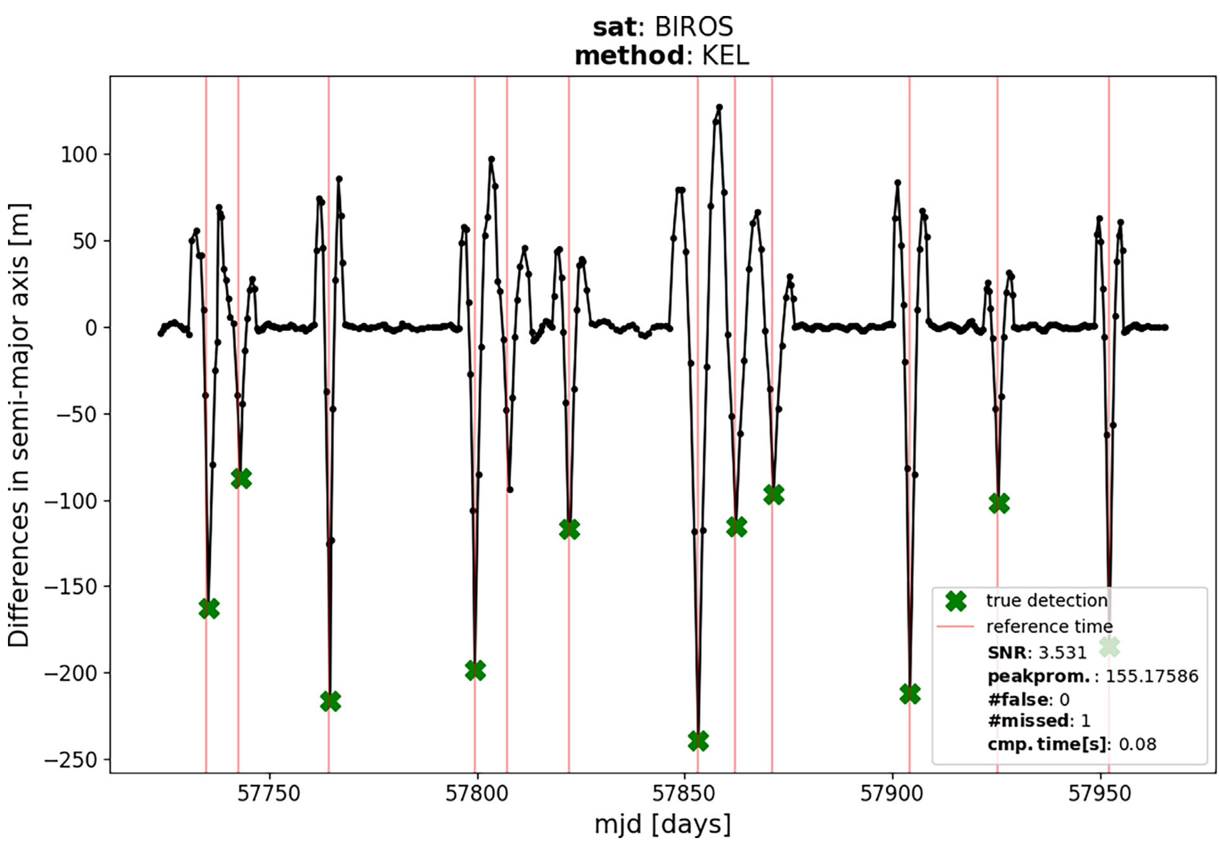

Fig. 6. Usage of peak prominence to detect manoeuvres in difficult scenarios. In the example, a series of orbit lowering manoeuvres performed by the DLR-GSOC satellite BIROS.

the Kelecy method (KEL) leads, on average, to a negative signal with some disturbing peaks on the positive side. In this case the topographic prominence can clearly replace two statistical thresholds, one for positive and one for negative values, without considering the upper peaks as erroneously detected manoeuvres.

6. Filter comparison through convex optimization

An optimizer for filter tuning has been developed, with the goal to fairly compare the detection performances of the LKF and the mean-longitude filter (MLF) to the KEL algorithm and the TCC. The detection methods, in fact, differ in terms of input tuning parameters, as listed in Table 1.

In order to guarantee that every technique is always providing its best detection performance, the optimal input-set of tuning parameters for each method, X_{opt}, has been obtained from an optimization process such that the loss function $L(Y)$ is minimized:

$$X_{opt} = (x_1, \cdots, x_n) : \min_X L(Y) \tag{11}$$

The loss function has been derived by incorporating metrics that are commonly employed in the field of pattern recognition and binary classification. An extensive list of these measures can be found in Tharwat (2018). The parameters in Eq. (12) characterise the confusion matrix of a binary classifier:

$$Y = (n_{miss}, n_{false}, n_{det}) \tag{12}$$

where n_{miss} is the number of missed detections, n_{false} the number of false detections, n_{det} the number of correctly detected manoeuvres. These quantities can be combined in the metrics Precision and Recall (Sokolova et al., 2006) expressed respectively in Eqs. (13) and (14).

$$Pr = \frac{n_{det}}{n_{det} + n_{false}} \tag{13}$$

$$Re = \frac{n_{det}}{n_{det} + n_{miss}} \tag{14}$$

The first quantity represents the proportion of manoeuvres that were correctly detected to the total number of detected manoeuvres (also including incorrect detections). The second represents the ratio between correctly classified manoeuvres to the total true number of manoeuvres (Sokolova et al., 2006; Tharwat, 2018). Precision and Recall can be further combined in their harmonic mean (Eq. (15)) defined often by the literature as F_1.

$$F_1 = \frac{2n_{det}}{2n_{det} + n_{false} + n_{miss}} \tag{15}$$

Since high values of F_1 indicate high classification performance, it has been selected by the authors as a key parameter for the definition of the loss function. This last has in fact been defined as:

$$L(Y) = \frac{1}{F_1} \tag{16}$$

The minimum of the scalar function expressed in Eq. (16) is found by means of a bi-directional line search as implemented in the modified Powell algorithm (Powell, 1964).

Another important metric that has been used within the context of this research is the signal-to-noise ratio SNR given by:

$$SNR = \frac{\mu(S) + \sigma(S)}{\mu(N) + \sigma(N)} \tag{17}$$

where $\mu(S)$ and $\sigma(S)$ are respectively the mean and the standard deviation of all the data-points above the detection threshold and $\mu(N)$ and $\sigma(N)$ are mean and standard deviation of all the data-points below the detection threshold. The SNR gives an indication of how well the peaks are defined with respect to the background noise. It has been used in the following sections as a discrimination factor for scenarios in which the detection is straightforward and different methods reach the same value of the loss function.

7. Detection results for LEO regime

Firstly, the performances of the introduced techniques are tested for the LEO regime. Table 2 gives an overview of the data-sets employed for testing. Different scenarios have been chosen by the authors to challenge the detection.

Table 1
Tuning parameters of each method for the optimization process.

Method	Input tuning parameter	Description
KEL	Window span: $\boldsymbol{w}$	Number of datapoints characterizing the smoothing sliding window.
	Polynomial order: $\boldsymbol{k}$	Order of the polynomial regression used to smooth data.
TCC	Number of propagations: $\boldsymbol{n}$	Number of times each datapoint has been propagated to the next for computing the expected variance.
	Window size: $\boldsymbol{s}$	Width of the kernel function to perform the LOWESS algorithm.
	Polynomial order: $\boldsymbol{o}$	Order of expected variance interpolant curves.
LKF and **LKF_S**	Process noise: $\boldsymbol{Q}$	Noise level associated to the dynamical propagation model.
	Measurement noise: $\boldsymbol{R}$	Noise level associated to the measurement process.
	Initial state covariance: $\boldsymbol{P}_0$	Covariance matrix associated to the initial state (initial guess for the Kalman estimation process).
MLF	Scaling factor: $\boldsymbol{\tau}$	Factor that scales the width of the kernel function to perform the LOWESS algorithm.

Table 2
LEO satellites data-set.

Data-set no.	Satellite name	Time period	No. of manoeuvres	Data kind
#1	ENVISAT (IN-PLANE)	08-04-2022 to 15-02-2006	59	TLEs
#2	ENVISAT (OUT-OF-PLANE)	08-04-2022 to 15-02-2006	11	TLEs
#3	TOPEX	30-09-1992 to 15-07-2022	22	TLEs
#4	BIROS	01-12-2016 to 01-08-2017	12	Operator orbits (GSOC)

The data-sets differ in typical manoeuvre magnitudes and in orbit data kinds.

For the test cases in Table 2, the optimization process finds the best set of tuning parameters, indicated in Table 1, to get the optimal performance for each detection method. Once the minimum of the loss function expressed in Eq. (12) is found, the detection results are plotted and illustrated to the reader only for the case of data-set #1. The results of the overall analysis are summarized in Table 4, in Section 9.

Figs. 7 and 8 show respectively the detection with the KEL and the TCC methods following the selection of optimal tuning parameters. The rate of change of the semi-major axis has been chosen to perform the detection. Each vertical line represents the reference time of manoeuvre defined as the instant of mid-burn duration. Manoeuvres detected by the solver are flagged with a green cross, while red crosses are indicating false detections. It is worth noticing how the output of the optimizer brings the same detection signals presented in the original research of Kelecy et al. (2007) and Lemmens and Krag (2014)).

Figs. 9–11 show respectively the detection case of an LKF of 1st order (LKF1), an LKF of 1st order with RTS smoothing (LKF_S) and an LKF of 2nd order (LKF2) for the same data-set.

Fig. 12 presents the overall results for all the scenarios summarized in Table 2. The histogram chart provides the minimum value of the loss function normalised with respect to the corresponding SNR and to the worst-case scenario for each specific case. The normalisation relative to the worst scenario ensures that the best performance is always provided by the method associated by the lowest bar, while the worst has always a value equal to one. The normalisation relative to the SNR, on the other hand, accounts for all the cases where different methods achieve the same minimum of the loss function. For the case of BIROS, the KEL method gives the worst detection, while the LKF1 outperforms the TCC and the LKF2. For this

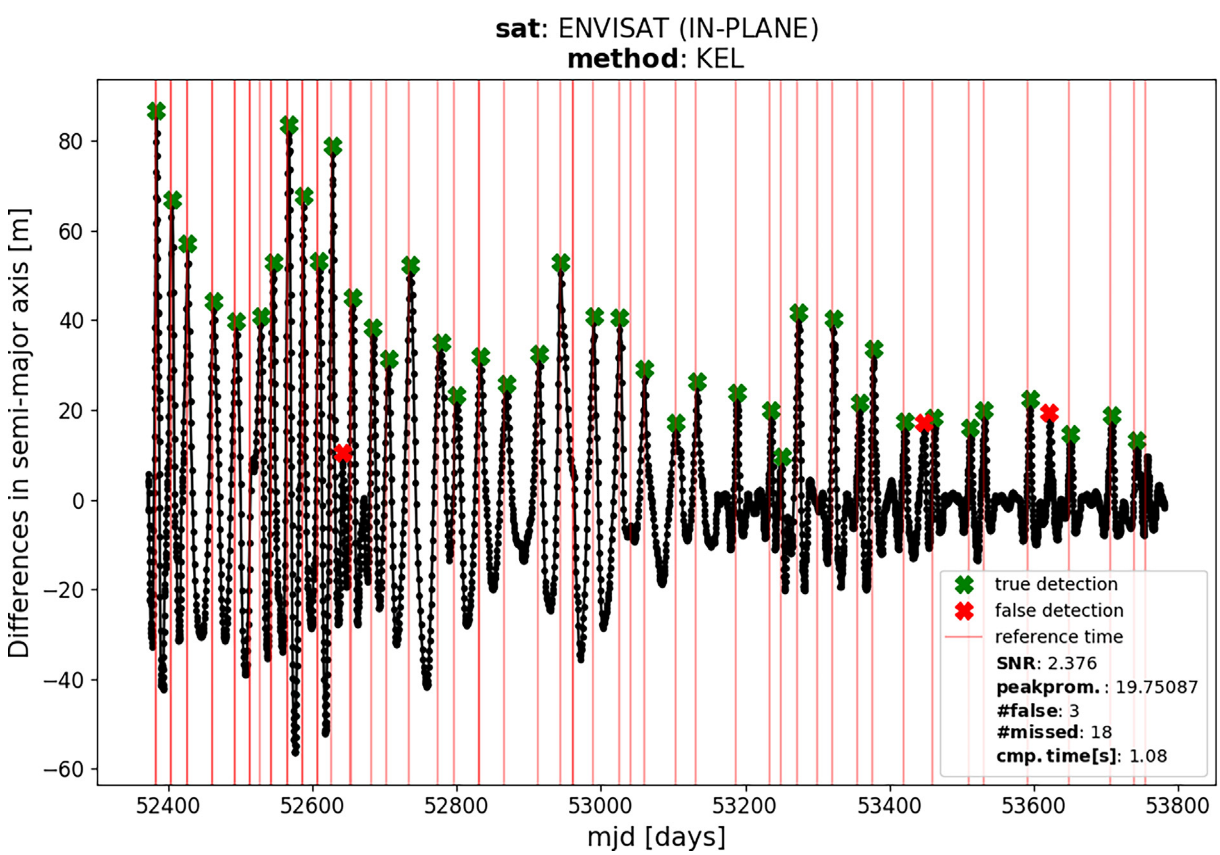

Fig. 7. Manoeuvre detection of Envisat in-plane manoeuvres (data-set #1) with the KEL method.

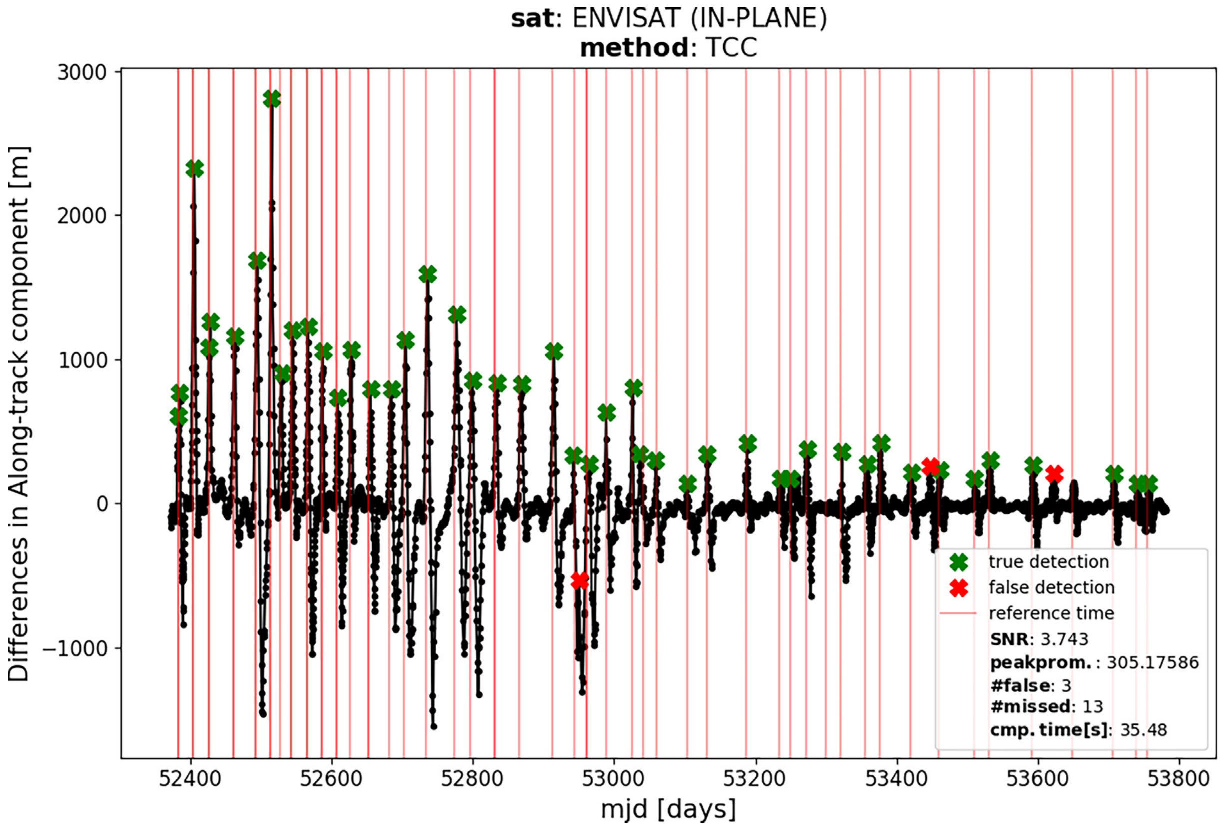

Fig. 8. Manoeuvre detection of Envisat in-plane manoeuvres (data-set #1) with the TCC method.

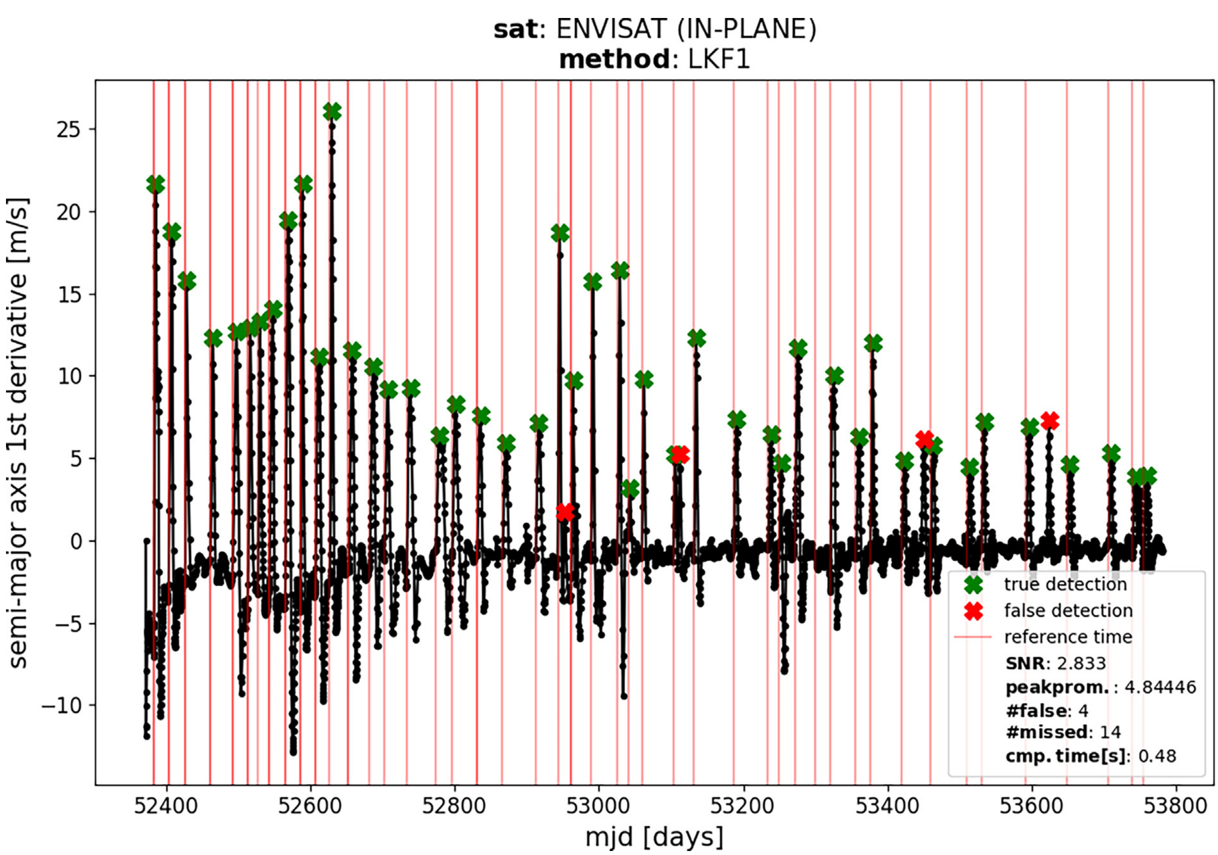

Fig. 9. Manoeuvre detection of Envisat in-plane manoeuvres (data-set #1) with the LKF1 method.

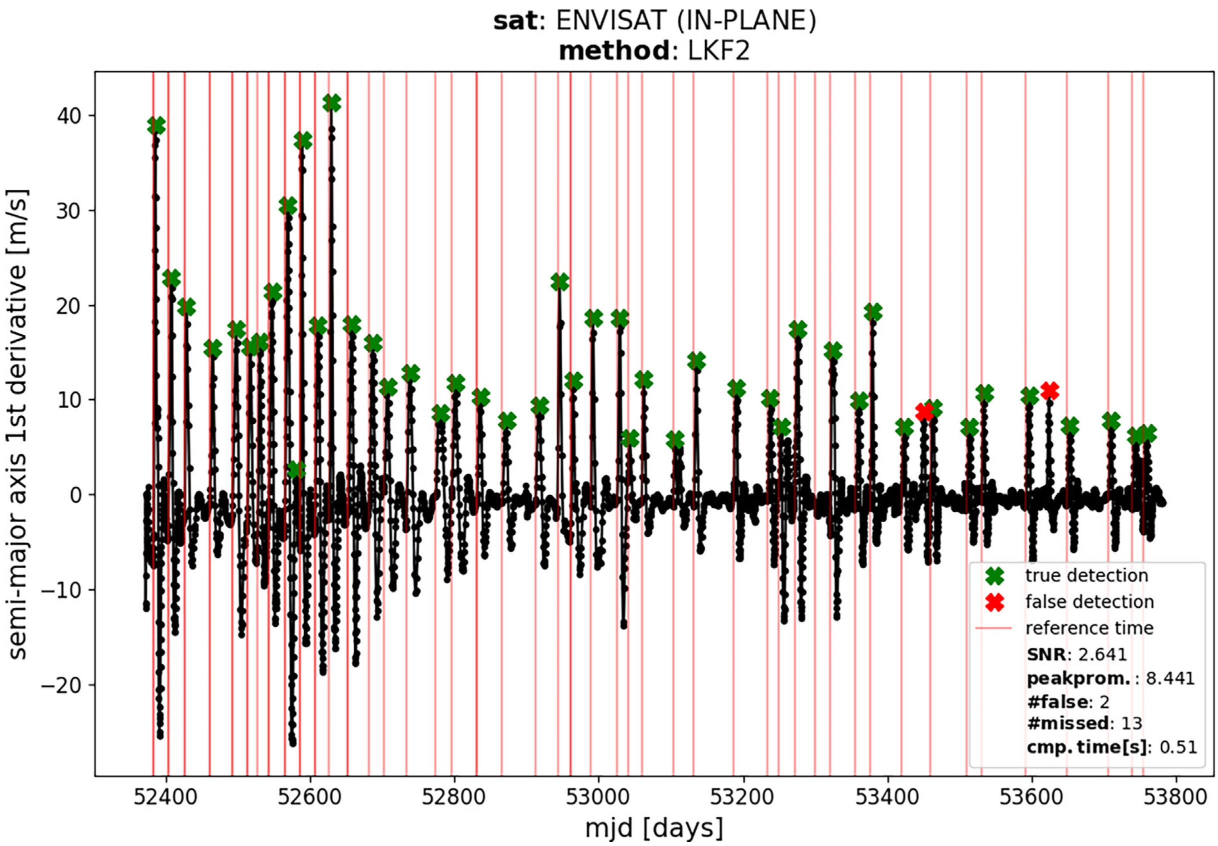

Fig. 10. Manoeuvre detection of Envisat in-plane manoeuvres (data-set #1) with the LKF2 method.

specific case considering a quadratic dependency between states in the propagation step does not benefit the detection, providing a lower sigma-to-noise ratio. The LKF_S ranks behind the TCC, but with the advantage of being way faster in term of computational time. A smoother in this case, given the highly accurate orbit of the operator, has a non-beneficial averaging effect that reduces the peak prominence, deteriorating the detecting performances. For TOPEX, since the data-set is noisier, LKF_S and LKF2 work better. The TCC, for this kind of scenarios, struggles as it needs a higher number of propagations to adjust for the local variability of the data. For ENVISAT, the situation does not change in term of noise level, since TLEs were considered. For the out-of-plane manoeuvres scenario, the LKF2 and the LKF_S seem to predominate thanks to their tendency to reject noise. The in-plane manoeuvres of ENVISAT represent a more challenging situation, where orbit corrections are more frequent and less pronounced. Again, the noise cancellation of the backward smoother has a strong impact, but also the ephemeris comparison of the TCC appears to be really effective. Summarising, when the noise level is high, it is in fact suggested to run a backward smoother to account for more variability in the tracked signal. In general, the newly introduced techniques are outperforming the already existing methods. For easy detection scenarios a low order for the LKF is best suited for detection. On the contrary, for noisy scenarios, increasing the order of the propagation-step dynamics or running a backward smoother is way more beneficial.

The data-set of ENVISAT in plane has been also used as a demonstrative example to show the utility of Receiver Operating Characteristics (ROC) curves (Bradley, 1997) when comparing manoeuvre detection classifiers. ROC curves are a powerful tool commonly used in the field of decision making to easily show different working points of binary classifiers. As the discrimination threshold of these last varies, the Recall, also known as False Positive Rate (FPR), and the True Positive Rate (TPR) are computed (Tharwat, 2018). For our specific application the TPR is defined in Eq. (18) as:

$$FPR = \frac{n_{false}}{n_{false} + TN} \tag{18}$$

where TN stands for True Negative and represents the number of occurrences of correctly non-detected manoeuvres. TN has been computed by subtracting the number of real executed manoeuvres to the total number of TLE records. Since the behaviour of a classifier is usually analysed by considering only one discrimination threshold, for each manoeuvre detection technique we selected the most relevant tuning parameter while keeping the others to their initial optimum. No further optimisation of the remaining parameters is performed and therefore the optimal performance is not established in each operating point

Please cite this article as: A. Zollo and M. Weigel, Comparison of satellite manoeuvre detection methods based on timeline of orbit elements, Advances in Space Research, https://doi.org/10.1016/j.asr.2023.10.032

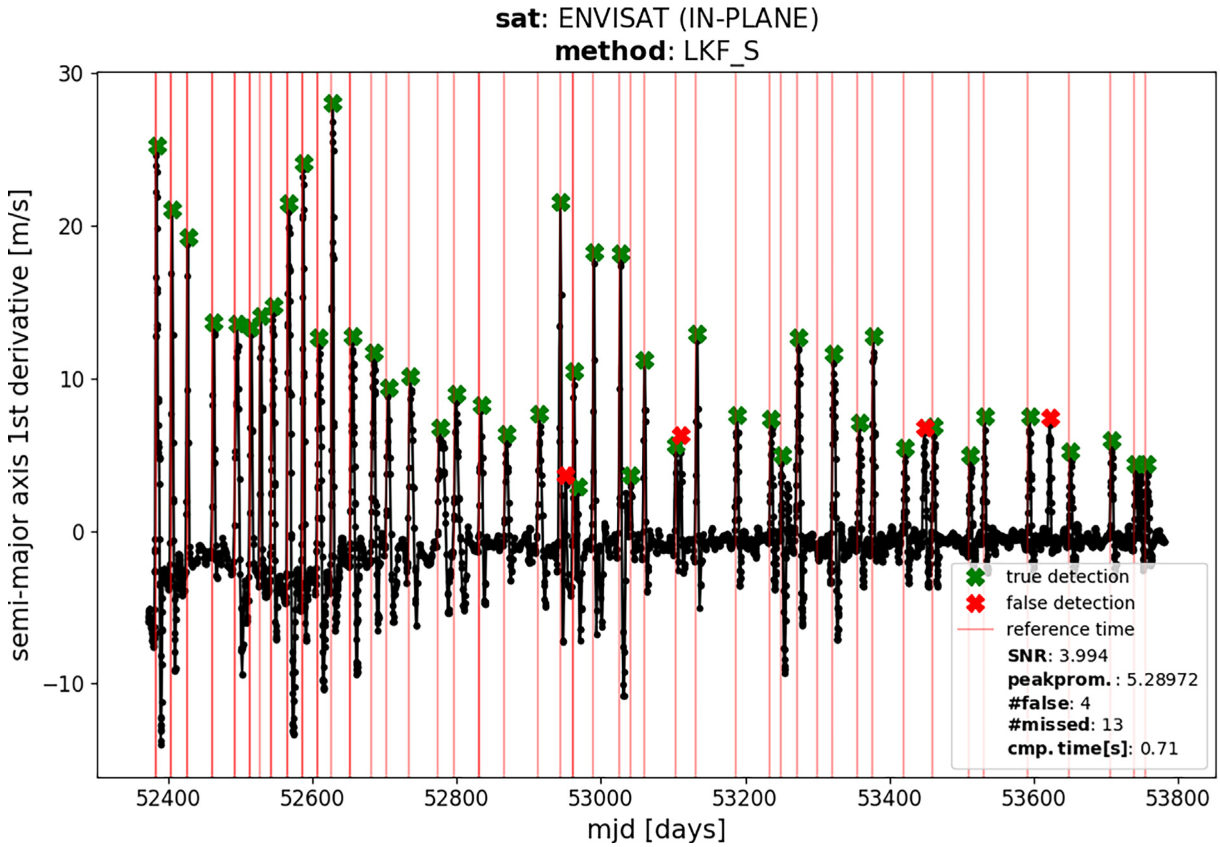

Fig. 11. Manoeuvre detection of Envisat in-plane manoeuvres (data-set #1) with the LKF_S method.

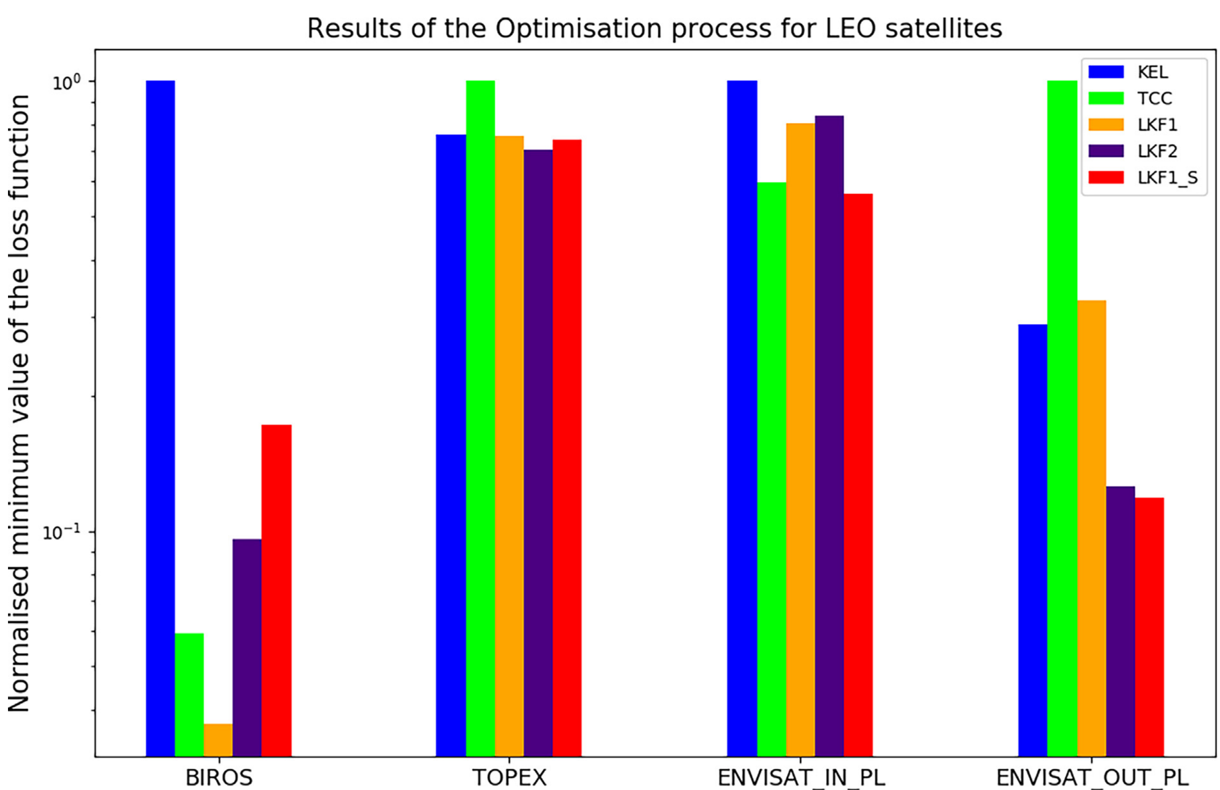

Fig. 12. Comparison of relative loss values for data-sets #1, #2, #3, #4 of LEO satellites.

of the ROC curve. Being more specific, the results shown in Fig. 13 have been obtained by varying for the TCC and KEL the window size and the window span respectively, while for the LKF based methods the process noise. As a curve approaches the ideal point in $(0, 1)$, the performance of the detection methods improves across a wider range of values for the selected tuning parameter. As expected, for the data-set of ENVISAT, the TCC and the LKF_S are not only outperforming their competitors when they are optimally tuned, but also for a broader spectrum of window size and process noise values. The zoom shows the optimum tuning set of each technique corresponding to the minimum of the loss function. In contrast to what has been shown in Fig. 12, it can be noted that the optimum of the TCC ranks above the one of the LKF_S, even if only slightly. The root cause of this is the partial characterisation of the problem, with the behaviour studied for only one tuned parameter. In reality, each point on the curve needs an optimisation process on its own to really assess the performances of the classifiers across a wider range of operating conditions. For this application, the ROC curve would, in fact, be a discrete, piece-wise defined, multi-dimensional surface that makes the comparison cumbersome.

8. Detection results for GEO regime

As done for the LEO case, the same analysis has been performed on the GEO data-sets introduced in Table 3. For this testing campaign, again, two sources of orbit information were taken into consideration: TLEs and operator orbits. For the particular case of the satellite EDRS-C, the situation is again split in the analysis of in-plane and out-of-plane manoeuvre detection.

A detailed summary of the results is again reported in Table 4. For the GEO regime, the characteristic manoeuvre magnitudes allow the usage of normalized residuals defined in Eq. (6) as signal on which to perform the peak detection. Signal detection performed on the semi-major axis rate of change in this case would increase on average the noise of the results. An example is provided in Fig. 14, where the detection is performed on the in-plane manoeuvres of EDRS-C. The reader is invited to note that for this case 18 manoeuvres are systematically missed (see Table 4) by all methods. This is due to the particular manoeuvre strategy implemented by this mission. The satellite longitude drift and eccentricity are controlled by a bi-pulse strategy. The couple of burns are almost consecutive for an orbit determination point of view and, as a consequence, no datapoints in between pulses are present in the timeline of estimated orbits. Despite this, well-defined peaks are arising in correspondence of the second burn mean manoeuvring

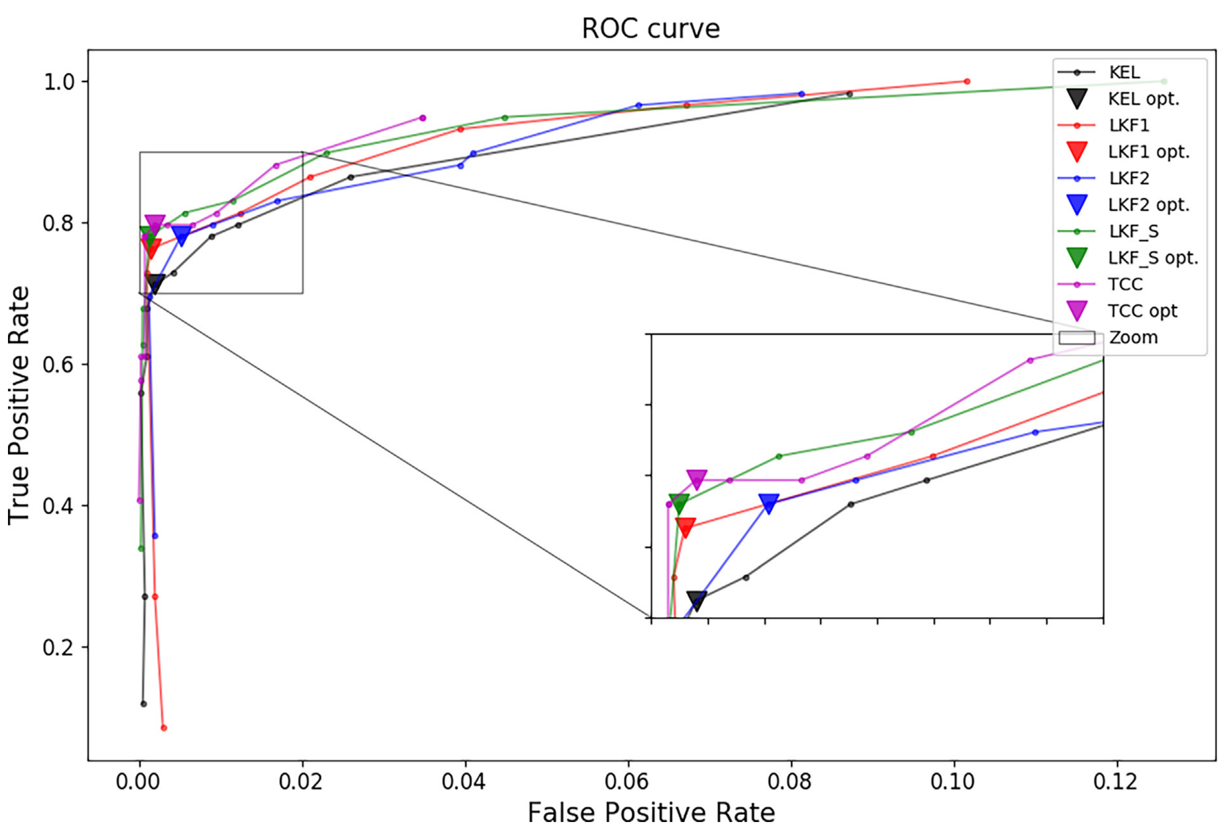

Fig. 13. Receiver Operating Characteristics (ROC) curves for ENVISAT (IN-PLANE).

Table 3
GEO satellites data-set.

Data-set no.	Satellite name	Time period	No. of manoeuvres	Data kind
#1	EDRS-C (IN-PLANE)	2019-12-02 to 2020-11-20	37	Operator orbits (GSOC)
#2	EDRS-C (OUT-OF-PLANE)	2019-12-02 to 2020-11-20	11	Operator orbits (GSOC)
#3	METEOSAT-10	2018-03-12 to 2020-02-01	10	TLEs

Table 4
Summary of results for all data-sets in both LEO and GEO regimes.

LEO REGIME							
Data-set no.	No. man	method	No. true det.	No. missed	No. false det.	SNR	cmp. time [s]
#1	59	**KEL**	41	18	3	2.38	0.76
		TCC	46	13	3	3.74	29.77
		LKF1	45	14	4	2.83	0.51
		LKF2	46	13	2	2.64	0.51
		LKF_S	46	13	4	3.99	0.72
#2	11	**KEL**	11	0	0	2.54	0.82
		TCC	10	1	6	4.35	31.65
		LKF1	11	0	0	2.25	0.51
		LKF2	11	0	0	5.77	0.49
		LKF_S	11	0	0	6.41	0.67
#3	22	**KEL**	21	1	1	2.09	0.92
		TCC	21	1	15	3.09	40.91
		LKF1	22	0	2	2.81	0.49
		LKF2	21	1	1	4.05	0.44
		LKF_S	21	1	0	6.55	0.67
#4	12	**KEL**	11	1	0	4.263	0.07
		TCC	12	0	0	16.10	1.2
		LKF1	12	0	0	25.76	0.04
		LKF2	12	0	0	9.85	0.05
		LKF_S	12	0	0	5.55	0.07
GEO REGIME							
#1	37	**KEL**	19	18	0	3.97	0.07
		TCC	19	18	0	1.00	3.27
		LKF1	19	18	0	1.28	0.03
		LKF2	19	18	0	3.31	0.03
		LKF_S	19	18	0	1.00	0.04
		MLF	19	18	0	1.00	2.42
#2	10	**KEL**	10	0	1	1.66	0.03
		TCC	10	0	0	4.98	1.62
		LKF1	10	0	1	68.44	0.01
		LKF2	10	0	1	2928.23	0.02
		LKF_S	10	0	0	1.79	0.03
#3	10	**KEL**	10	0	2	4.32	0.23
		TCC	9	1	2	62.46	5.09
		LKF1	10	0	1	23.03e5	0.17
		LKF2	10	0	2	343.289	0.17
		LKF_S	10	0	2	5.25	0.23
		MLF	10	0	2	9.71	0.49

time, leading to a straightforward detection of the remaining pulses.

Fig. 15 provides an overview of the results for the GEO data-sets. Again, the normalised values of the loss function show the relative performance of each technique. Contrary to the LEO section, data-set #1 and #3 allow testing also for the MLF described in Section 4.

For EDRS-C in-plane manoeuvres, LKF1 and LKF2 ensure lowest values of the loss function outperforming the competing methods. The detecting signal worsens when introducing the smoothing. As mentioned before, this happens because the noise level is very low for precise operator orbits and the averaging effect of the smoother when running backwards on the data decreases the SNR. Also, for EDRS-C out-of-plane manoeuvres and METEOSAT-10, signal-to-noise ratios produced by the LKFs are one or two orders of magnitude higher than those of the KEL and TCC methods. Regarding the mean longitude filter, it ranks generally between TCC and KEL, providing similar detection performance. This is somehow expected since it belongs to the same algorithm category that processes differences in the orbital state between datapoints. As a

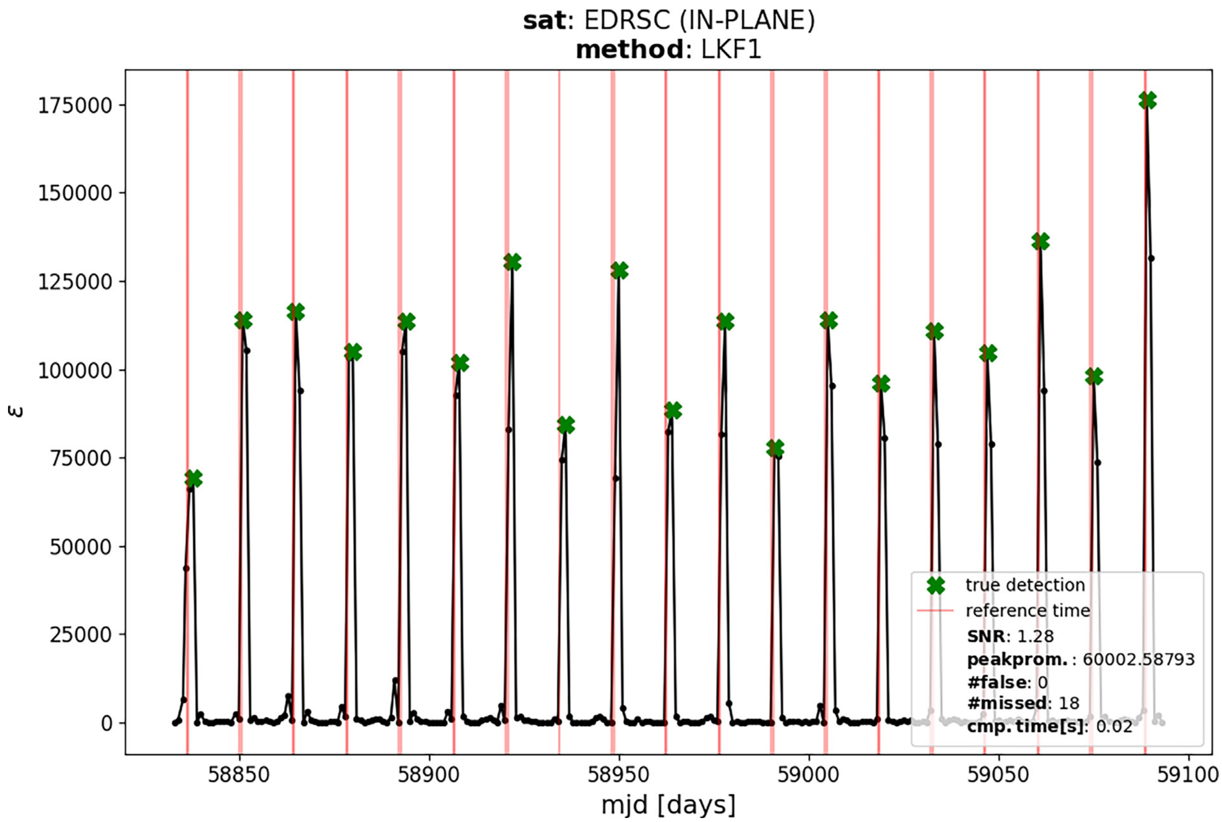

Fig. 14. Manoeuvre detection of EDRS-C in-plane manoeuvres (data-set #1) with LKF1 method.

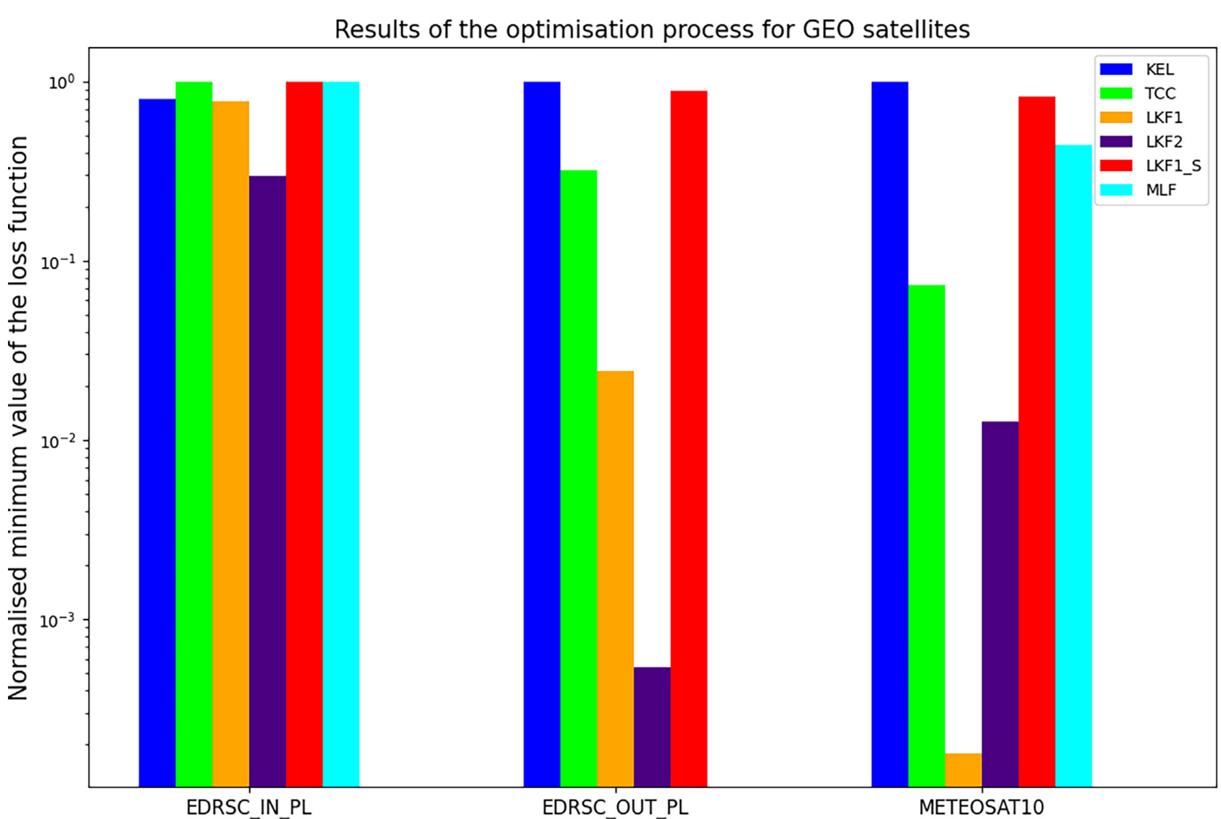

Fig. 15. Comparison of relative loss values for data-sets #1, #2, #3 of GEO satellites.

Please cite this article as: A. Zollo and M. Weigel, Comparison of satellite manoeuvre detection methods based on timeline of orbit elements, Advances in Space Research, https://doi.org/10.1016/j.asr.2023.10.032

general remark, it is important to note how the usage of the squared and normalised residuals improves significantly the detection. In fact, in contrast to the quantities implemented in the other techniques, the usage of ε gives intrinsically positive signals with high values of SNR.

9. Overall result outline and additional considerations

Table 4 summarizes the testing campaign for all the data-sets presented in Tables 2 and 3. For both orbital regimes the LKFs are providing a lower value for the loss function, indicating, overall, better performances with respect to the already existing methods. In general, for data-sets with less noise, e.g. operator orbits, a first or second-order LKF are sufficient for generating a high signal-to-noise ratio and corresponding manoeuvre detectability. For highly noisy data, as for the case of TOPEX, the averaging effect of the smoother provides a better detection performance. With regards to the MLF, it ranks in term of performance at the same level as the competitors, since it is belonging to the same category of manoeuvre detection algorithms. Despite this, it has the advantage of solving the intrinsic problematic of geostationary satellites manoeuvre patterns described in Section 4.

Fig. 16 shows another important factor to consider when performing off-line manoeuvre detection analysis: the computational time. For both LEO and GEO regimes the execution time in seconds is illustrated on a logarithmic scale. The overall situation shows the TCC to be the most time-consuming technique, always having longer runtimes by two orders of magnitude. This is a typical disadvantage of all the off-line manoeuvre detection methods that involve complex propagation dynamics. The LKFs are generally providing higher computational speed. The KEL method has a computational time comparable to the LKF with backward smoothing, i.e. roughly twice the time of a nominal LKF. The MLF provides smaller computational times with respect to TCC.

10. Conclusions

Within the framework of this research, two novel methods for detecting manoeuvres in a timeline of already-estimated orbits are introduced. Both techniques are well suited to support off-line studies and SSA catalogue maintenance. They can be employed for understanding historical manoeuvre trends and strategies and to support sensor scheduling. Their usage can also be beneficial for the process of spacecraft mass estimation or, more generally, to carry out statistical studies on the in-orbit popula-

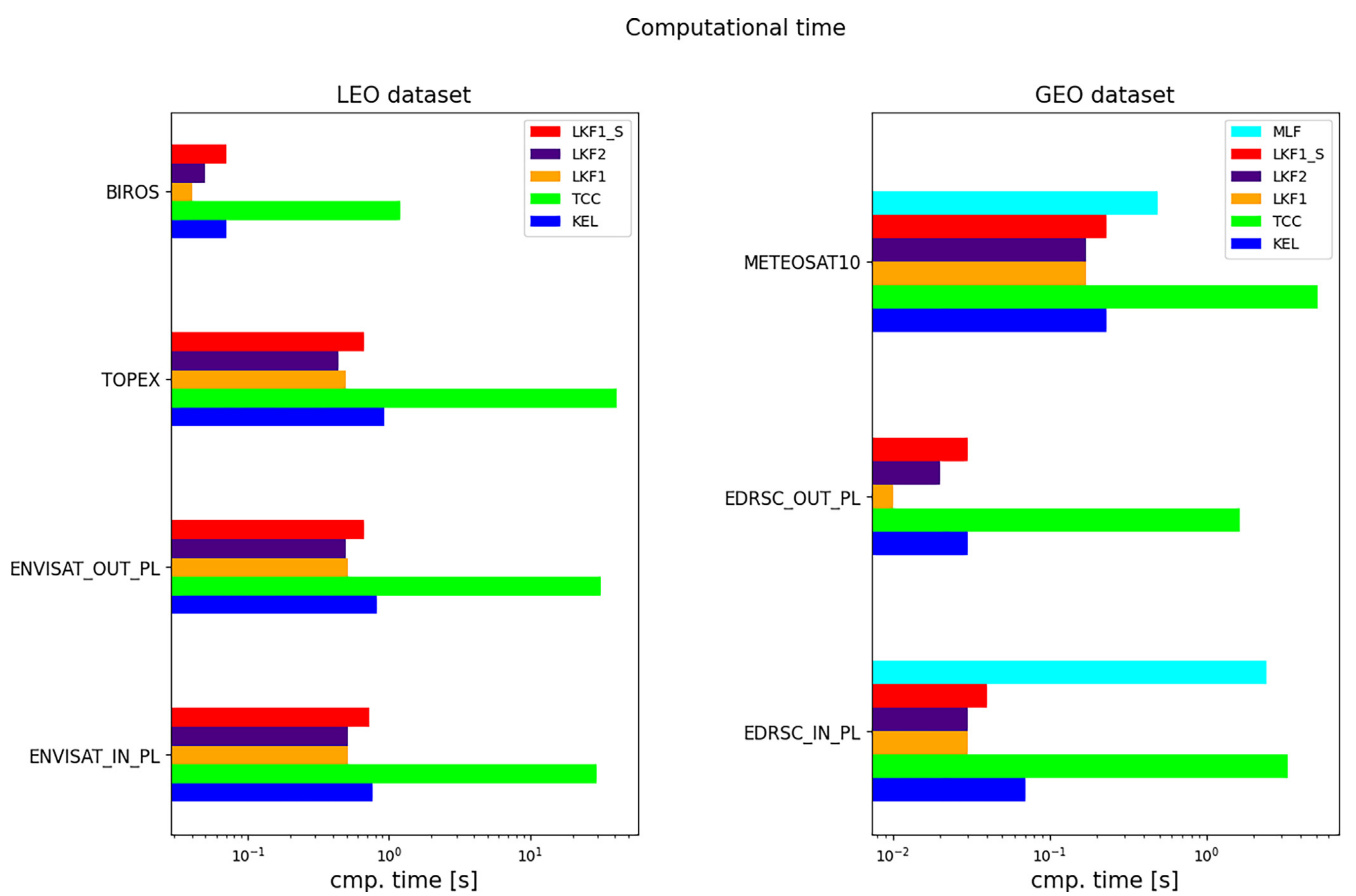

Fig. 16. Comparison of computational time for LEO and GEO data-sets.

Please cite this article as: A. Zollo and M. Weigel, Comparison of satellite manoeuvre detection methods based on timeline of orbit elements, Advances in Space Research, https://doi.org/10.1016/j.asr.2023.10.032

tion of active and non-active objects. The first method is based on a discrete-time LKF to smooth noisy data and to detect orbit changes. The filter ingests sequentially a timeline of orbital element and manoeuvres can be spotted by analyzing two different quantities: the filter squared and normalized residuals or the rate of change of the tracked orbit elements. In addition, it has been shown that its formulation can be extended for highly noisy data by introducing a backward RTS smoother. The second method is instead specifically related to the East-West control of a GEO satellite. It employs a locally weighted regression algorithm to smooth differences in mean longitude. It has been shown that studying the mean longitude overcomes the problem of in-plane bi-pulse patterns for cases in which the satellite is brought back to the same semi-major axis before the manoeuvre. For all the methods the authors have shown the potential of using the peak prominence as an indicator to the manoeuvre detection, in contrast to statistical limits based on the signal.

The introduced manoeuvre detection techniques are then compared to two already existing methods proposed respectively by Kelecy et al. (2007) and Lemmens and Krag (2014). Their intrinsic implementation differences have raised the problem of how different methods can be compared fairly. To solve this, the authors put in place an optimization process that ensures that each technique is always working optimally, despite different test cases. To each method and data-set corresponds a value of the loss function used to rank the detection performances. The proposed optimizer is also a valid alternative to the classical trial-and-error or sensitivity studies to tune the detection algorithms which, in the end, are strongly data dependent. Once the optimal set of tuning parameters is found for a reference scenario, the same detection settings can be applied for catalogued objects with similar orbits, manoeuvre strategies and orbit determination processes.

A testing campaign is performed to assess the behavior of the newly introduced techniques with regards to different scenarios such as different orbital regimes, different orbital data, different level of noises and different manoeuvre magnitudes. Overall, the LKFs are performing better than the competitors' algorithms. When the noise level of the orbit timeline is high, a greater order of the filter is advised along with a backward smoothing. For low noise levels, assuming a first-order linear dynamics is deemed enough to get outstanding detection results. Additionally, it has been shown that the simple mathematical formulation of the techniques presented in this research leads to low computation times and less error prone software implementation.

Declaration of competing interest

The authors declare that they have no known competing financial interests or personal relationships that could have appeared to influence the work reported in this paper.

References

Águeda, A., Aivar, L., Tirado, J., Dolado, J.C., 2013. In-orbit lifetime prediction for LEO and HEO based on orbit determination from TLE data. 6th European Conference on Space Debris, volume 723, p. 61.

Bar-Shalom, Y., Xiao-Rong, L., Kirubarajan, T., 2001. Estimation with Applications to Tracking and Navigation. Wiley, New York.

Bergmann, C., Zollo, A., Herzog, J., Fiedler, H., Schildknecht, T., 2021.. Integrated Manoeuvre detection and estimation using nonlinear Kalman filters during orbit determination of satellites. 8th European Conference on Space Debris, Darmstadt, Germany, 20–23 April 2021.

Bergmann, C., Zollo, A., Herzog, J., Fiedler, H., Schildknecht, T., 2022.. Detection of satellite manoeuvres using non-linear Kalman filters on passive-optical measurements. 73rd International Astronautical Congress (IAC), Paris, France, 18–22 September 2022.

Bradley, A.P., 1997. The use of the area under the ROC curve in the evaluation of machine learning algorithms. Pattern Recogn. 30 (7), 1145–1159.

Cleveland, W., Dec 1979. Robust locally weighted regression and smoothing scatterplots. J. Am. Stat. Assoc. 74 (368), 829–836.

Folcik, Z.J., Cefola, P.J., Abbot, R.I., 2008. GEO maneuver detection for space situational awareness. Adv. Astronaut. Sci. 129, 523–550.

Herzog, J., Fiedler, H., Schildknecht, T., 2017. Using conjunction analysis methods for Manoeuvre detection. 7th European Conference on Space Debris, Darmstadt, Germany, 2017, 18–21 April.

Kalman, R.E., 1960. A new approach to linear filtering and prediction problems. J. Basic Eng. 82, 35–45.

Kelecy, T., Hall, D., Hamada, K., Stocker, D.M., 2007. Satellite Maneuver detection using two-line element (TLE) data. Advanced Maui Optical and Space Surveillance (AMOS) Technologies Conference, Maui, Hawaii, USA, 2007, 12–15 September.

Labbe, R., 2020. Kalman and bayesian filters in python. https://github.com/rlabbe/Kalman-and-Bayesian-Filters-in-Python.

Lemmens, S., Krag, H., 2014. Two-line-elements-based Maneuver detection methods for satellites in low Earth orbit. J. Guid. Control Dyn. 37 (3).

Li, H., 2014. Geostationary Satellites Collocation. Springer.

Li, T., Li, K., Chen, L., 2018. New manoeuvre detection method based on historical orbital data for low earth orbit satellites. Adv. Space Res. 62 (3), 554–567.

Li, T., Li, K., Chen, L., 2019. Maneuver detection method based on probability distribution fitting of the prediction error. J. Spacecraft Rock. 56 (4), 1114–1120.

Mahalanobis, P.C., 1936. On the generalised distance in statistics. Proc. Natl. Instit. Sci. India 2 (1), 49–55.

Montenbruck, O., Gill, E., 2001. Satellite Orbits: Models, Methods, and Applications. Springer.

Mukundan, A., Wang, H.-C., 2021. Simplified approach to detect satellite Maneuvers using TLE data and simplified perturbation model utilizing orbital element variation. Appl. Sci. 11 (21), 10181.

Patera, R.P., 2008. Space event detection method. J. Spacecraft Rock. 45 (3), 554–559.

Powell, M.J.D., . An efficient method for finding the minimum of a function of several variables without calculating derivatives. Comput. J. 7 (2), 155–162.

Rauch, H., Tung, F., Striebel, C., 1965. Maximum likelihood estimates of linear dynamic systems. AIAA J. 3 (8), 1445–1450.

Schild, M., Noomen, R., 2022. Sun-synchronous spacecraft compliance with international space debris guidelines. Adv. Space Res., 2022 https://doi.org/10.1016/j.asr.2022.07.011.

Siminski, J., Hauke, F., Tim, F., 2017. Correlation of Observations and Orbit Recovery Considering Maneuvers. AAS/AIAA Space Flight Mechanics, San Antonio, Texas, USA.

Sokolova, M., Japkowicz, N., Szpakowicz, S., 2006. Beyond accuracy, f-score and roc: a family of discriminant measures for performance evaluation. In: Australian Joint Conference on Artificial Intelligence. Springer, pp. 1015–1021.

Song, W.D., Wang, R.L., Wang, J., 2012. A simple and valid analysis method for orbit anomaly detection. Adv. Space Res. 49 (2), 386–391.

Swartz, R., Coggi, J., McNeill, J., 2010. A swift sift for satellite event detection. In: AIAA/AAS Astrodynamics Specialist Conference, p. 7527.

Tharwat, A., 2018. Classification assessment methods. Appl. Comput. Inf. 17 (1), 168–192.

Weigel, M., Meinel, M., Fiedler, H., 2015. Processing of optical telescope observations with the space object catalogue BACARDI. 25th International Symposium on Space Flight Dynamics ISSFD.

Zhao, Y., Zhang, K., Bennett, J., Sang, J., Wu, S., 2014. A method for improving two-line element outlier detection based on a consistency check. Proceedings of the Advanced Maui Optical and Space Surveillance (AMOS) Technologies Conference, Maui, Hawaii.

Zollo, A., 2020. Satellite Maneuver Detection and Estimation using Optical Measurements. Master Thesis. Institut Supérier de l'Aéronautique et de l'Espace, Toulouse. https://elib.dlr.de/137623/.